Article

DFT Study of Oxygen Ion Migration in Mg-Doped Cubic Zirconia

Zhussupbek M. Salikhodzha [1] , **Guldari B. Bairbayeva** [1,*] , **Anatoli I. Popov** [1,2] , **Raigul N. Kassymkhanova** [1] , **Keleshek B. Zhangylyssov** [1] , **Elena Popova** [3,*] and **Marina Konuhova** [2]

1   Institute of Physical and Technical Sciences, Faculty Transport and Energy, L.N. Gumilyov Eurasian National University, 13 Kazhymukan St., Astana 010000, Kazakhstan; salikhodzha_zhm@enu.kz (Z.M.S.); popov@latnet.lv (A.I.P.); suleimen_rn@enu.kz (R.N.K.); keleshek92@yandex.ru (K.B.Z.)
2   Institute of Solid-State Physics, University of Latvia, LV-1063 Riga, Latvia; marina.konuhova@cfi.lu.lv
3   Department of Physics, University of Maryland, College Park, MD 20742-4111, USA
*   Correspondence: bairbayeva_gb_3@enu.kz (G.B.B.); epopova@umd.edu (E.P.)

Abstract

This work presents a theoretical investigation of ionic conductivity in cubic zirconia (c-ZrO_2) doped with magnesium, using density functional theory (DFT) with the hybrid B3LYP functional as implemented in the CRYSTAL23 software package. It was found that the spatial arrangement of magnesium atoms and oxygen vacancies significantly affects the energy barriers for oxygen ion migration. Configurations with magnesium located along and outside the migration path were analyzed. The results show that when Mg^{2+} is positioned along the migration trajectory and near an oxygen vacancy, stable defect complexes are formed with minimal migration barriers ranging from 0.96 to 1.32 eV. An increased number of Mg atoms can lead to a further reduction in the barrier, although in certain configurations the barriers increase up to 3.0–4.6 eV. When doping occurs outside the migration path, the energy profile remains symmetric and moderate (0.9–1.1 eV), indicating only a weak background influence. These findings highlight the critical role of coordinated distribution of Mg atoms and oxygen vacancies along the migration pathway in forming efficient ion-conducting channels. This insight offers potential for designing high-performance zirconia-based electrolytes for solid oxide fuel cells and sensor applications.

Keywords: zirconium dioxide; doping; DFT; oxygen migration; energy barrier

Academic Editor: Robert A. Jackson

1. Introduction

Zirconium dioxide (ZrO_2) is a promising oxide material widely used in solid oxide fuel cells, lithium-ion batteries, photocatalysis, and optoelectronics due to its high thermal and chemical stability, ionic conductivity, and mechanical strength [1–4]. ZrO_2 nanoparticles exhibit activity in the photodegradation of organic pollutants [2] and are employed in batteries to enhance anode stability and prevent degradation [3,4]. In addition, ZrO_2 is in demand in catalysis and as a dielectric material in thin-film structures [5–8], highlighting its versatility and importance among modern functional materials [9–14]. The ZrO_2 is also one of the most promising materials for nuclear engineering [15–19], and when doped, it is an effective phosphor for many luminescent applications [20–22].

ZrO_2 is a wide-bandgap semiconducting oxide with a polymorphic structure that exists under atmospheric pressure in three allotropic modifications [23,24]: monoclinic (m-ZrO_2) [25], tetragonal (t-ZrO_2), and cubic (c-ZrO_2). The monoclinic phase (baddeleyite) is thermodynamically stable at room temperature, while the transitions to the tetragonal

and cubic modifications occur at 1478 K and 2650 K, respectively [26,27]. Controlling the phase stability of ZrO_2 is crucial for its application in ceramics, including solid oxide fuel cells (SOFCs), dental materials, and jewelry [28–37].

Pure zirconium dioxide is characterized by a low concentration of oxygen vacancies, which limits its ionic conductivity. The activation energy for ion transport is determined by the sum of the vacancy formation energy and the migration energy barrier. Various dopants are used to enhance conductivity and stabilize specific phases. The most common dopant elements include Yb [38], Ce [39,40], and Y [41], as well as Al, Ca, Eu, Mg, Na, Sc, and Tb [42]. For example, the addition of 10 mol% Sc stabilizes the cubic c-ZrO_2 phase, resulting in high ionic conductivity [43]. Doping with Al allows tuning of the bandgap width and enhances the absorption coefficient in the tetragonal phase of ZrO_2 [44], while lanthanide ions not only stabilize the ZrO_2 phase but also modulate its optical emission properties [45–49].

Doping ZrO_2 with magnesium oxide (MgO) leads to the formation of oxygen vacancies, which enhances ionic conductivity. Studies show that MgO doping affects the polymorphic transformations and mechanical properties of ZrO_2. It has been established that low concentrations of MgO stabilize the tetragonal phase, while higher concentrations promote the transition to the cubic phase. The strengthening of the material is associated with phase transitions, increased dislocation density, and the formation of intergranular MgO inclusions [50].

Previous DFT studies have shown that sulfur doping increases the formation energy of oxygen vacancies and raises the migration barrier, resulting in reduced ionic conductivity [51]. The effect of MgO on the radiation resistance of ZrO_2 was also investigated in [52], where it was demonstrated that an optimal concentration of 0.10 mol% MgO leads to the formation of a substitutional phase $Zr_{0.9}Mg_{0.1}O_2$, which reduces deformation and enhances the material's strength. Studies on the defect structure of ZrO_2 [53] revealed that polyalanines form chains of oxygen vacancies, which may act as conductive filaments in ReRAM devices, enabling resistive switching through oxygen migration. Moreover, doping ZrO_2 with impurity ions affects the system's total energy, contributing to phase stabilization and improved ionic conductivity, which is important for applications in solid oxide fuel cells [54].

Despite numerous studies on zirconia modeling, the question of how the spatial arrangement of Mg atoms relative to the oxygen migration path affects ionic conductivity remains unresolved. It is unclear whether substitution along the migration pathway enhances conductivity through direct interaction with vacancies or, conversely, creates obstacles due to local structural distortion.

In this work, a theoretical investigation of ionic conductivity in cubic zirconia (c-ZrO_2) stabilized with magnesium was carried out using density functional theory (DFT) with the hybrid B3LYP correlation-exchange (XC) functional. The study focuses on the influence of oxygen vacancies and the spatial positioning of magnesium dopants on the energy profile of oxygen ion migration. The scientific novelty of this work lies in the comparative analysis of two doping strategies and in identifying the decisive role of the local coordination environment in forming effective oxygen migration pathways, which can be applied in the design of next-generation oxide electrolytes.

2. Materials and Methods

The ideal crystal of cubic zirconium dioxide (c-ZrO_2) has a face-centered cubic structure with space group symmetry Fm-3m (225). The ZrO_2 crystal structure corresponds to a fluorite-type arrangement formed in the cubic space group Fm-3m. Zr^{4+} atoms are coordinated by eight O^{2-} atoms in a body-centered cubic configuration, with a Zr–O bond

length of 2.20 Å. Each O^{2-} ion is bonded to four equivalent Zr^{4+} atoms, forming an OZr_4 tetrahedral coordination polyhedron with shared angles and edges [55].

In this study, density functional theory (DFT) [56,57] was employed using the hybrid B3LYP [58,59] functional implemented in the CRYSTAL23 software package [60]. A $2 \times 2 \times 2$ supercell of cubic zirconia (c-ZrO_2) containing 96 atoms was used as the model system (see Figure 1). In all calculations, the following basis sets were employed: Zr—Zr_SC_HAYWSC-3111(32111df) G, O—O_8-411, and Mg—Mg_8-511d1G. All basis sets were taken from the CRYSTAL23 library. (https://www.crystal.unito.it/basis_sets.html, accessed on 30 August 2025). In CRYSTAL, restricted (closed shell) calculations are used by default, which is appropriate for ZrO_2 since Zr^{4+} and O^{2-} ions have fully filled outer shells and electrons are paired.
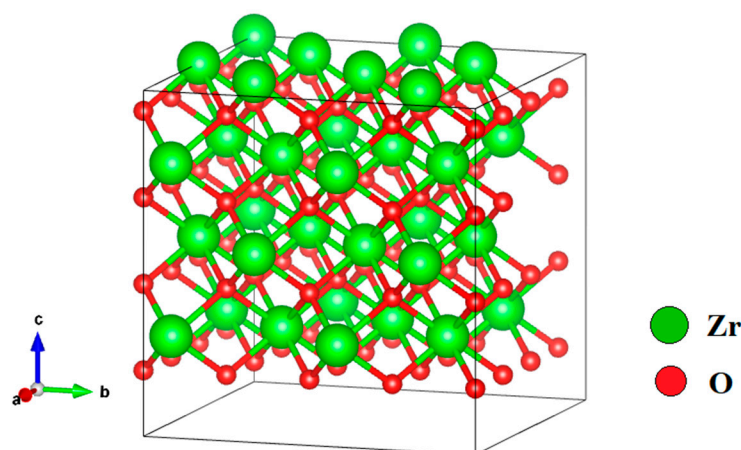

Figure 1. Structure of c-ZrO_2.

To calculate the structural and electronic properties, total energy calculations were performed without geometry optimization. The initial lattice parameter was set to a = 5.10 Å [61], and the calculated band gap was 5.28 eV, which is comparable to the experimental value of 6.1 eV [62].

To accurately model ionic conductivity in cubic zirconia (c-ZrO_2), the calculations were carried out without performing full geometry optimization of atomic positions and lattice parameters. This approach preserved the target structure required for subsequent studies of ionic transport. The system was modeled using density functional theory (DFT) with strict convergence criteria: an energy threshold of 10^{-6} eV, a gradient threshold of 4.5×10^{-4} eV/Å, and a maximum atomic displacement of 1.8×10^{-3} Å. These settings ensured high precision in calculating the structural and energetic characteristics of the system. Oxygen vacancies were created in the calculations by removing oxygen atoms from the lattice. To provide a clearer picture of how oxygen vacancies and Mg substitutions affect the crystal lattice, Table 1 summarizes the local distortions and the resulting average symmetries for different defect configurations. The data highlights the transition from the ideal cubic structure to tetragonal or rhombohedral distortions upon vacancy formation, as well as the restoration of cubic symmetry at higher Mg concentrations. It should be noted that these symmetrical changes are local in nature, while the overall bulk structure remains cubic since full geometric optimization was not performed.

Thus, the correlation between migration barriers and structural symmetry emphasizes that both the type and distribution of defects play a decisive role in defining ionic conductivity in ZrO_2-based systems.

These defects were modeled to investigate their key role in ionic conductivity, as they form possible migration pathways for oxygen ions in the material.

Table 1. Local symmetry changes in cubic ZrO_2 with oxygen vacancies and Mg substitutions (near and outside vacancy sites).

Configuration	Local Effect	Average Symmetry	Space Group	Lattice Change
$Zr_{32}O_{64}$ (ideal)	Perfect cubic lattice	Cubic	Fm-3m	a = b = c
$Zr_{32}O_{63}$ (1 V_O)	Zr shifts toward vacancy; distortion	Locally tetragonal	Local tetragonal/rhombohedral	Local anisotropy
$Zr_{32}O_{61}$ (3 V_O)	Vacancy chain $\langle 001 \rangle$; elongation	Tetragonal	$P4_2/nmc$	c/a > 1
Mg near V_O (1–3)	Mg–VO dipoles; stronger distortions; high Mg restores cubic	Tetragonal → Cubic-like	$P4_2/nmc$ → Fm-3m	c/a > 1 → ≈ 1
Mg outside V_O (1–3)	Weak background effect; lattice stable	Mostly cubic	Fm-3m	a ≈ b ≈ c

In addition, in crystalline materials, a distinction is usually made between stoichiometric and non-stoichiometric defects. The first group includes, for example, Frenkel and Schottky defects, where the overall cation-to-anion ratio is preserved despite local disorder. In contrast, oxygen vacancies in cubic ZrO_2 are non-stoichiometric defects, since their formation changes the cation-to-anion ratio and leads to a deviation from the ideal stoichiometry [63]. Magnesium dopants were introduced into the system by substituting some of the zirconium atoms, allowing the investigation of magnesium's influence on ionic conductivity. Magnesium in the structure can shift the positions of vacancies and create new defect pathways, affecting oxygen ion migration and, consequently, the material's conductivity.

These calculations involving magnesium doping and oxygen vacancies provide a basis for further analysis of ionic conductivity in c-ZrO_2, which is important for developing advanced materials for solid oxide fuel cells and other applications. The analysis of the system's total energy as a function of oxygen vacancy concentration and magnesium content allowed us to examine the influence of defects on the phase stability and electronic properties of zirconia.

3. Results

3.1. Investigation of the Electronic Properties of Magnesium-Stabilized Cubic Zirconia

It is well known that the creation of oxygen vacancies in ZrO_2 contributes to structural stabilization and enhances ionic conductivity. These vacancies are modeled from first principles by removing one or more oxygen atoms from the supercell.

The modeling is carried out using standard density functional theory (DFT) methods. Total and partial densities of electronic states (DOS and PDOS) are calculated using the hybrid B3LYP functional. The valence electron configurations are $4d^2 5s^2$ for zirconium and $2s^2 2p^4$ for oxygen. Oxygen vacancies are modeled within a cubic ZrO_2 supercell containing 96 atoms. The geometric parameters of the nearest atoms are not optimized.

As shown in Figure 2, in pristine ZrO_2, the valence band is primarily composed of oxygen 2p orbitals, with a maximum around −4.5 eV, while the conduction band starts above the Fermi level and includes contributions from Zr 4d states. Upon the creation of an oxygen vacancy, an additional narrow localized state appears near the bottom of the conduction band, associated with the remaining paired electron.

In the PDOS spectra (Figure 2), the formation of a single oxygen vacancy in ZrO_2 leads to the appearance of a localized state approximately 0.1 eV below the Fermi level. At the same time, the vacancy contributes negligibly to the valence band. The main contributions to the valence and conduction bands originate from oxygen (O 2p) and zirconium (Zr 4d) atoms, respectively. These findings align with the general model of defect state formation in oxide dielectrics and demonstrate the potential role of vacancies in enabling ionic conductivity.
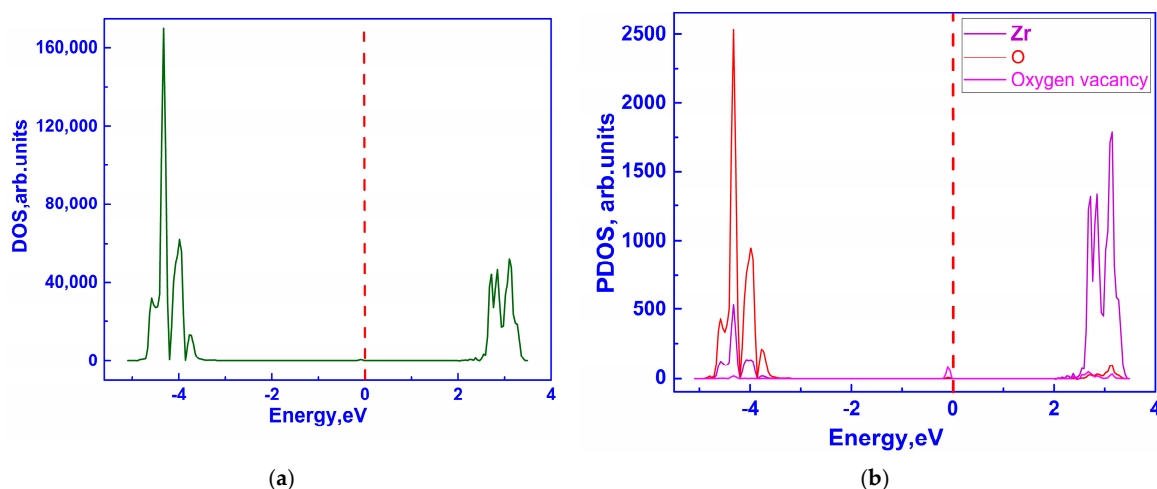
Figure 2. DOS (**a**) and PDOS (**b**) of $Zr_{32}O_{63}$.

With an increase in the concentration of oxygen vacancies in ZrO_2 to three per supercell, the total density of states retains the typical oxide profile with a wide band gap (Figure 3). However, in the PDOS projected onto the vacancy sites, a localized state appears within the band gap (approximately 0.1–0.5 eV below the Fermi level), associated with the defects. In the configurations shown in Figures 2 and 4, the removed oxygen atoms and the positions of Zr atoms substituted by Mg are illustrated in Figure 3.
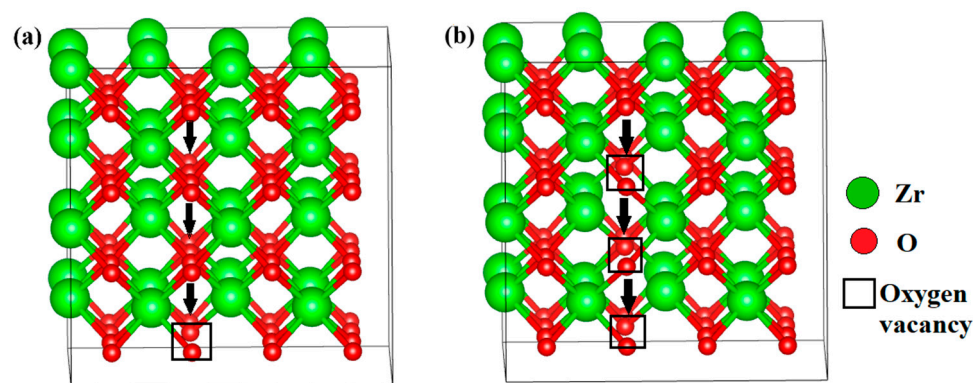

Figure 3. Structure of c-ZrO_2 with one oxygen vacancy (**a**) and with three oxygen vacancies (**b**) along the oxygen migration path.
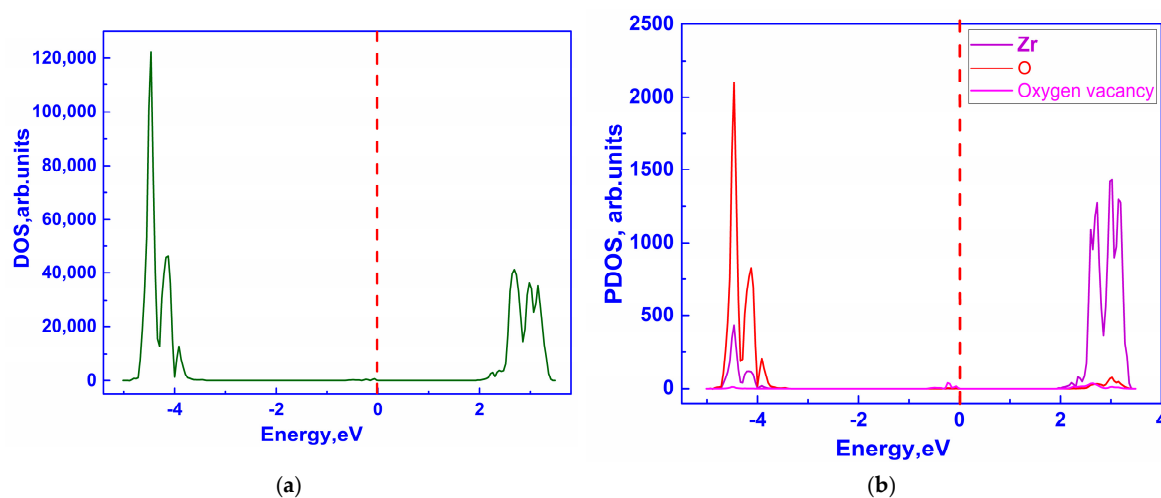

Figure 4. DOS (**a**) and PDOS (**b**) of $Zr_{32}O_{61}$.

The height and width of the peaks indicate an accumulation of defect states that maintain a discrete character, suggesting that the vacancies are spatially separated. This confirms their influence on ionic conductivity.

Figure 5 presents the total and partial density of states (DOS and PDOS) for a zirconia structure containing one magnesium substitutional atom and one oxygen vacancy. The upper part of the valence band is primarily formed by oxygen 2p electrons, while the conduction band is mainly composed of zirconium 4d electrons. As shown in the PDOS, magnesium contributes minimally to the electronic structure of the system, which is consistent with its Mg^{2+} electronic configuration and the absence of unoccupied d-states.
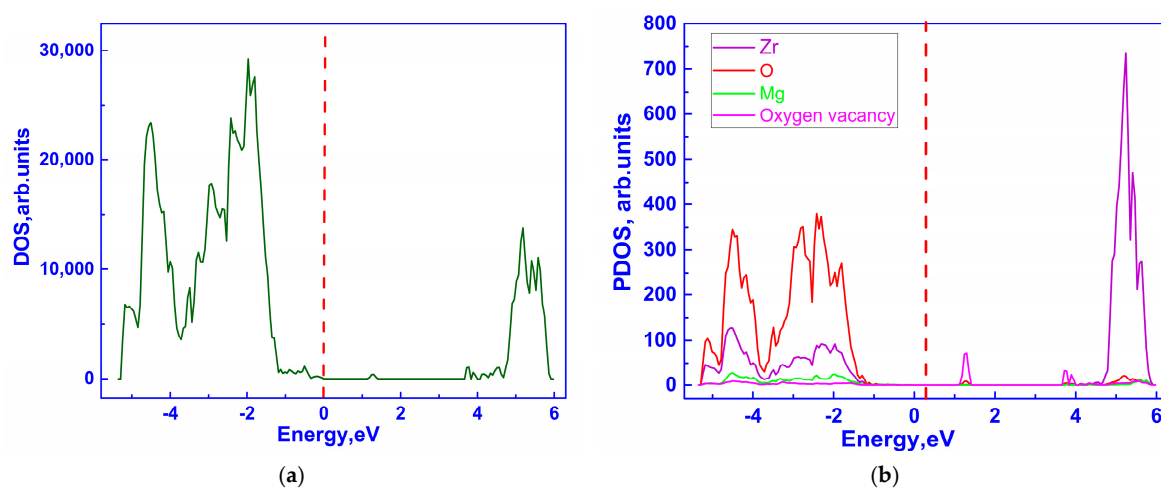

(a)   (b)

Figure 5. DOS (**a**) and PDOS (**b**) of $Zr_{31}Mg_1O_{63}$.

It is clearly observed that the defect states associated with the oxygen vacancy are in the lower part of the conduction band (approximately 1.3 eV above the Fermi level). The position of the oxygen vacancy state has shifted compared to the undoped system.

Figure 6 shows the total and partial density of states (DOS and PDOS) for a zirconia system containing two oxygen vacancies and two magnesium atoms. As in previous cases, the valence band is mainly formed by oxygen 2p orbitals, while the conduction band consists primarily of zirconium 4d states. The presence of oxygen vacancies leads to the formation of defect levels in the upper part of the band gap, which in this system are located closer to the conduction band edge—approximately 4.5–5.5 eV above the Fermi level.
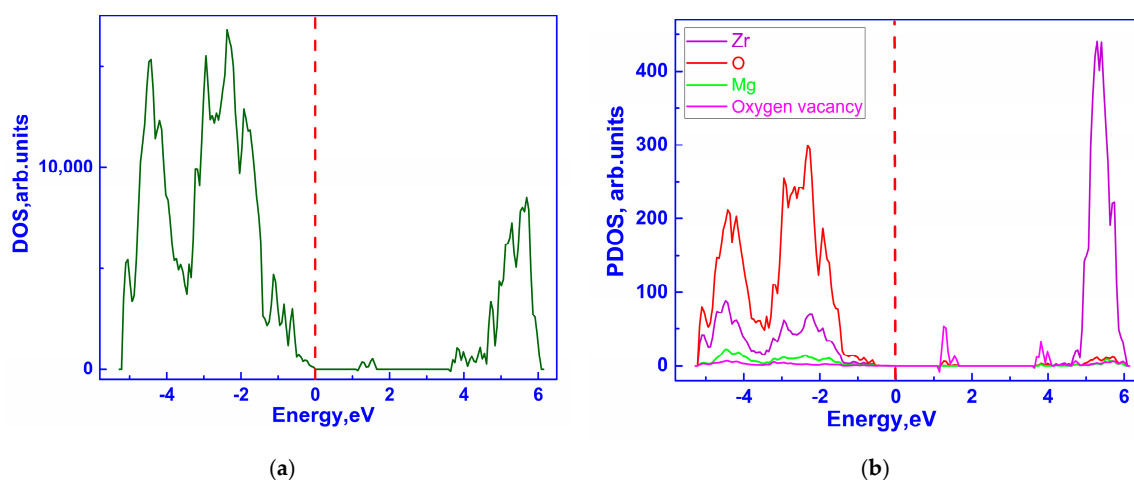

(a)   (b)

Figure 6. DOS (**a**) and PDOS (**b**) of $Zr_{30}Mg_2O_{62}$.

These defect states exhibit greater intensity than in the case with a single vacancy, indicating a cumulative effect of electron localization as the number of vacancies increases. The contribution of magnesium atoms near the Fermi level remains minimal, confirming their role as compensating dopants that influence charge neutrality but do not directly participate in the formation of the band structure. Thus, double magnesium substitution stabilizes the vacancies, shifting their associated states into the conduction band region.

Figure 7 presents the total and partial density of electronic states (DOS and PDOS) for a zirconia system containing three oxygen vacancies and three magnesium atoms. The total DOS shows a characteristic separation between the valence and conduction bands with a wide band gap. As seen in the PDOS, the contribution from oxygen vacancies forms a clearly defined narrow state located near the bottom edge of the conduction band, approximately 5.5–6.0 eV above the Fermi level.
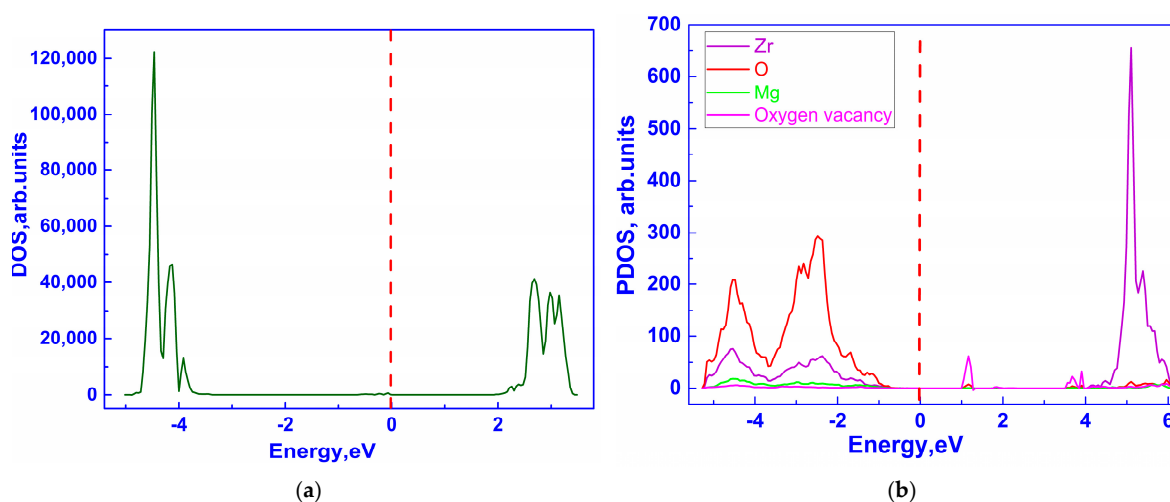

Figure 7. DOS (**a**) and PDOS (**b**) of $Zr_{29}Mg_3O_{61}$.

This indicates that as the concentration of vacancies increases, the energy level of the associated states shifts upward while maintaining a localized character. Additional magnesium substitution compensates for the excess charge, but the contribution from Mg remains minimal in both the valence and conduction bands. Thus, an increase in the number of defects enhances localization effects and may promote the formation of new channels for ionic conduction.

The atomic configurations corresponding to Figures 5–7, indicating the removed oxygen atoms and the positions of Zr atoms substituted by Mg, are illustrated in Figure 8.
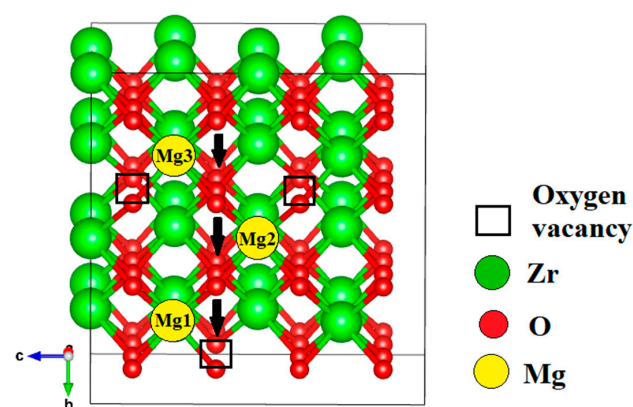

Figure 8. Oxygen migration along the trajectory with substitution of one, two, and three Zr atoms by Mg in c-ZrO_2.

An analysis of the total and partial density of states (DOS and PDOS) was conducted for ZrO_2 systems with one and three oxygen vacancies and varying numbers of Mg atoms. It was shown that the electronic structure is strongly dependent on the defect configuration.

In the system with a single vacancy, a localized state appears below the Fermi level, which may hinder ionic conductivity. The addition of one Mg atom shifts this state above the Fermi level and reduces its intensity, indicating charge compensation and state delocalization, thereby promoting improved oxygen mobility.

With an increase in the number of Mg atoms and vacancies to 2 and 3, further suppression of localized states is observed, while the contribution of Mg to the valence and conduction bands remains minimal, confirming its role as a charge compensator.

In the case of three vacancies without magnesium, pronounced unoccupied states are detected above the Fermi level—an indication of electronic traps. Their disappearance upon Mg introduction highlights the stabilizing effect of substitution.

Thus, configurations with a $Mg:V_O$ ratio close to 1:1 are the most effective for enhancing ionic conductivity by eliminating localized states and creating favorable pathways for oxygen migration. The results are consistent with literature data on perovskites [64,65] and emphasize the importance of targeted defect engineering in designing ZrO_2-based ion-conducting materials.

3.2. Investigation of Ionic Conductivity

Defects significantly influence the chemical and physical properties of metal oxides. Point and bulk defects often determine their catalytic, electrical, optical, and mechanical activity. Surface oxygen vacancies play a key role in heterogeneous catalysis. The oxygen vacancy formation energy on the surface ($E_o vac$) serves as an important parameter for predicting the catalytic properties of oxide materials.

To model an oxygen vacancy, one oxygen atom was removed from the supercell. The vacancy formation energy was calculated using the following expression:

$$E^F = E^d + E_O - E^p \tag{1}$$

where E^F—is the oxygen vacancy formation energy, E^d—is the total energy of the defective system, E_O—is the energy of an isolated oxygen atom, and E^p—is the total energy of the pristine (defect-free) system.

The oxygen vacancy formation energy ($E_o vac$) is an important parameter that determines the catalytic activity of metal oxides. Estimating these energies can support the development of promising catalysts using data-driven approaches. In the present study, $E_o vac$ values were determined for c-ZrO_2. It is known that $E_o vac$ is strongly influenced by the band gap width, lattice formation energy, and electron affinity.

The oxygen vacancy formation energy was calculated as the difference between the total energies of the defective supercell and the ideal crystal, considering the chemical potential of an oxygen atom, defined as the energy of a single O atom in its ground state.

The calculated oxygen vacancy formation energy is 12.6 eV, which is consistent with the typical overestimation of bond strength inherent to hybrid functionals. Since all subsequent calculations (including substitutional defects and defect complexes) were performed using the B3LYP functional, the use of this value ensures methodological consistency and allows for a reliable comparison of the relative energetic characteristics of different configurations.

3.2.1. Ionic Conductivity via Oxygen Vacancy-Mediated Oxygen Ion Migration

In this study, we examined the mechanism of oxygen migration in the defective structure of c-ZrO_2. A 96-atom supercell was constructed, in which one oxygen atom was initially removed to create a vacancy. Subsequently, an oxygen atom from the upper layer

was gradually displaced in 0.2 Å steps until it filled the oxygen vacancy at approximately 2.5 Å. This process was repeated for other layers of the structure (Figure 9, curve 1). At each step, the total energy of the system was calculated.
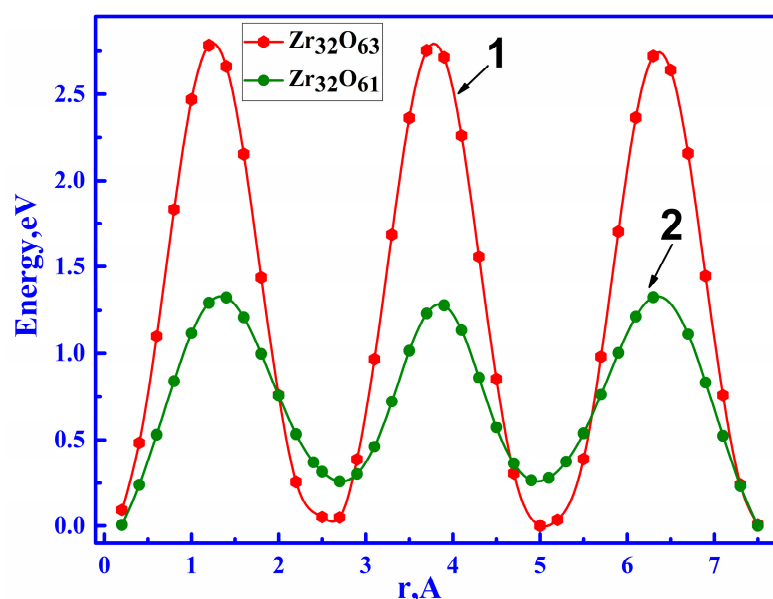

Figure 9. Dependence of the relative total energy of the system on the distance in the c-ZrO_2 structure with one oxygen vacancy (1) and three oxygen vacancies (2).

In the graph presented here and in subsequent analyses, the vertical axis represents the relative total energy of the system. It was found that the system's energy reaches a minimum when the oxygen atom occupies the vacancy and increases when it is near zirconium atoms. The dependence of the total energy on the oxygen atom's position exhibits a sinusoidal pattern, indicating the presence of periodic energy barriers and stable configurations within the structure. Figure 9 shows the energy profile along the oxygen ion migration path in defective cubic zirconia (c-ZrO_2) through vacancy sites. Curve 1 in Figure 9 corresponds to the migration of an oxygen ion into a single vacancy site (Figure 3a), while curve 2 represents migration through three oxygen vacancies (Figure 3b). The energy maxima observed at distances of 1.2–1.4 Å, 3.7–3.9 Å, and 6.3 Å indicate energy barriers that arise when the oxygen atom passes through a zirconium plane, interacting with Zr atoms and increasing the system's energy

The energy minimum, observed at 2.5 Å, 5 Å, and 7.5 Å, corresponds to positions where the oxygen atom sequentially occupies vacant sites, leading to system stabilization and energy minimization.

A comparison of the migration barriers for an oxygen ion in a structure with one vacancy (2.7 eV) and along a path with three vacancies (1.32 eV) reveals a reduction of 1.4 eV.

It should be noted that aligning multiple oxygen vacancies along a single trajectory is statistically unlikely. Nevertheless, the results confirm that the formation of oxygen vacancies significantly lowers the energy barriers for oxygen migration, thereby enhancing the material's ionic conductivity.

3.2.2. Ionic Conductivity of ZrO_2 Stabilized with MgO Aligned Along the Migration Path

To assess the effect of doping on the stability and ionic conductivity of zirconia, the energetic characteristics of systems containing one, two, and three magnesium atoms substituting zirconium atoms near a pre-existing oxygen vacancy were calculated. The total energy of the system consistently decreased with an increasing number of magnesium atoms:

−173,907.27 eV for one Mg, −176,028.56 eV for two, and −178,150.40 eV for three, indicating an increase in the thermodynamic stability of complex defects $Zr_{32-x}Mg_xO_{64-x}$ with higher dopant concentrations. These values are significantly lower than the energy of the system with a single vacancy (−169,733.80 eV) and the undoped system (−1,395,245.93 eV), confirming the energetic favorability of forming complex defects.

The substituting Mg^{2+} atoms aligned along the oxygen migration path lie in the same (100) crystallographic plane. This arrangement contributes to stabilizing the system containing oxygen vacancies (Figure 8).

In Figure 10a, the profile of the relative total energy during oxygen migration in the $Zr_{31}Mg_1O_{63}$ system (with one Mg atom aligned along the migration path) shows a shift in the positions of energy minima and maxima compared to the undoped structure. The graph illustrates the energy variation as a function of the oxygen ion's displacement coordinate.
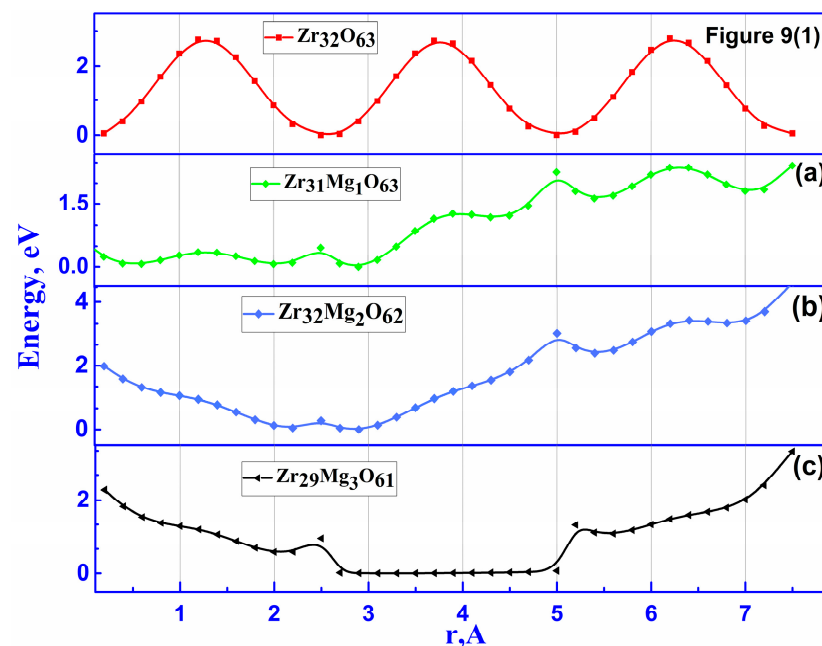

Figure 10. Dependence of the total energy of the system on the oxygen migration distance with substitution of one (**a**), two (**b**), and three (**c**) Zr atoms with Mg in c-ZrO_2. The top graph (previously labeled as Figure 9(1)) corresponds to the structure $Zr_{32}O_{63}$ with one oxygen vacancy.

At the points corresponding to vacancies (2.5 Å, 5.0 Å, and 7.5 Å), where deep minima were ideally expected, local maxima are instead observed: 0.462 eV, 2.264 eV, and 2.424 eV, respectively. This indicates that the Mg^{2+} ion located near the trajectory disrupts the symmetry of the potential curve and distorts the local electrostatic field. In the initial segment (0–2 Å), the energy gradually decreases, reaching a minimum of 0.067 eV at 2.0 Å, but then instead of further decreasing, it rises. At 3.7–3.9 Å and 6.3–6.4 Å, where the oxygen ion passes near zirconium, the energy increases to 1.26 and 2.37 eV, respectively. Similarly, when passing through the Mg-Zr planes (1.2–1.4 Å), the energy is approximately ~0.35 eV, which corresponds to the energy maximum in the undoped system with oxygen vacancies.

From the dependence of the system's total energy on the distance with one magnesium atom, it is seen that the total energy is lower compared to pure ZrO_2, indicating the thermodynamic stability of the defect structure. In the migration within the initial structure with a single oxygen vacancy, the maximum barriers reach ~2.7 eV. Thus, magnesium doping leads to a decrease in the total energy of the system and a reduction in migration barriers, although it is accompanied by a shift in critical points and a disruption of the migration path symmetry.

In Figure 10b, the dependence of the total energy of the system on the oxygen ion migration distance in the $Zr_{30}Mg_2O_{62}$ structure, where two zirconium atoms are replaced by magnesium along the migration path, is shown.

In the interval from 0.2 to 2.5 Å, a monotonic decrease in energy from 1.98 to 0.27 eV is observed with a local minimum of 0.048 eV at 2.2 Å and an absolute minimum (0 eV) at 2.9 Å. The minima at 2.2–2.9 Å are explained by the stable localization of oxygen near the vacancy.

Values at 1.4 Å and 3.9 Å, corresponding to the passage of oxygen through the Mg–Zr and Zr–Zr coordination planes, are characterized by local energy bends: at 1.4 Å, the energy is 0.774 eV, and at 3.9 Å—1.18 eV. This indicates the interaction of oxygen with nearby magnesium and zirconium atoms, creating local distortions in the electrostatic field of the lattice.

At 5.0 Å (the second vacancy), there is a sharp energy rise to 3.03 eV, indicating an increase in the potential energy of the electrostatic field. The oxygen ion exits the potential well corresponding to the vacancy and crosses the zirconium plane (at 5.4 Å—energy 2.39 eV). The maximum barrier of 4.62 eV is observed at 7.5 Å, which is associated with the completion of the migration path.

In Figure 10c, the dependence of the reduced total energy of the $Zr_{29}Mg_3O_{61}$ system corresponding to the oxygen ion migration along a trajectory with three magnesium ions is shown. In the initial region (0.2–2.5 Å), where the ion passes through the magnesium–zirconium planes, the energy gradually decreases from 2.27 eV to 0.96 eV. From 2.7 Å to 4.7 Å, a deep potential well is observed with energy ranging from 0.01664 eV to 0.03447 eV, which corresponds to the ion passing near Mg ions. However, when exiting this region (r > 5 Å), as the oxygen begins to leave the Mg influence zone and approaches the zirconium planes, the energy sharply increases. At 5.2 Å, the energy is 1.32 eV and continues to rise to 3.31 eV at 7.5 Å. Despite the relatively high final barrier, the system with three magnesium atoms exhibits the lowest total energy among all studied configurations, indicating its high stability. This emphasizes that with increasing Mg concentration, the system becomes more stable, but the electrostatic field becomes less symmetric, and the barriers may increase again in certain regions.

The analysis revealed that local substitution of zirconium atoms with magnesium near an oxygen vacancy has a significant impact on both the thermodynamic stability of the structure and the energy profile of oxygen ion migration. As the number of Mg atoms increases, the total energy of the system decreases consistently, indicating the formation of more stable configurations: −173,907.27 eV (1 Mg), −176,028.57 eV (2 Mg), −178,150.4 (3 Mg).

However, migration energy profiles exhibit a complex dependence on the number and arrangement of the dopant atoms (Table 2). With one Mg atom, the energy barriers shift but remain moderate compared to the undoped system (2.7 eV). In the case of two Mg atoms, deep potential wells are formed, but the end of the migration path shows a sharp energy increase up to 4.62 eV, indicating hindered migration. The third configuration, with three Mg atoms, offers the best stabilization of oxygen near the vacancy (energies ~0 eV), but is also accompanied by a rise in the energy barrier to 3.3 eV at the later stage of migration.

Table 2. Energy barriers for oxygen migration in c-ZrO_2 with different numbers and arrangements of Mg atoms.

Doping Configuration	Number of Mg	Min. Barrier, eV	Max. Barrier, eV
$Zr_{31}Mg_1O_{63}$	1	0.4	2.4
$Zr_{30}Mg_2O_{62}$	2	0.5	3.1
$Zr_{29}Mg_3O_{61}$	3	0.8	1.32

Thus, optimal ionic conductivity is achieved by balancing the number and spatial arrangement of dopant atoms: excessive magnesium can enhance local stabilization but may disrupt the uniformity of the migration channel, increasing energy barriers at the final stages of migration.

3.2.3. Ionic Conductivity of ZrO_2 Stabilized with MgO with Spatially Distributed Mg Ions

As a continuation of the investigation into the effect of magnesium doping on ionic conductivity in cubic zirconia (c-ZrO_2), a series of models were examined in which Mg atoms substituted zirconium atoms outside the oxygen ion migration trajectory. In the structures with Mg doping positioned away from the migration path, the magnesium atoms replace zirconium in various planes, primarily oriented along (001) and (100). Two Mg^{2+} ions are localized within the same (001) plane at z = 2.5645 Å, while the first Mg atom is displaced to the plane at z = 7.6936 Å, corresponding to another parallel (001) plane. This arrangement of magnesium ions, removed from the migration trajectory, eliminates their direct interaction with oxygen vacancies and limits their effect on the total system energy to background electrostatic influences (Figure 11).
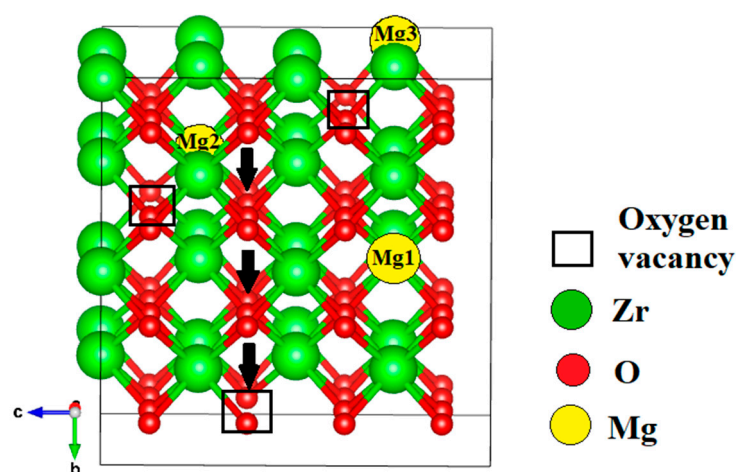

Figure 11. Oxygen migration with substitution of one, two, and three Zr atoms by Mg outside the migration trajectory in c-ZrO_2.

Three configurations were selected for calculation: $Zr_{31}Mg_1O_{63}$, $Zr_{30}Mg_2O_{62}$, and $Zr_{29}Mg_3O_{61}$, in which one, two, and three Mg atoms, respectively, substitute zirconium atoms outside the oxygen ion migration path, thus avoiding direct interaction with vacancies. The total energies of these systems were −173,905.54 eV, −176,760.58 eV, and −178,149.75 eV, respectively. This indicates that increasing MgO concentration contributes to thermodynamic stabilization.

From Figure 12a, corresponding to the $Zr_{31}Mg_1O_{63}$ configuration, the overall shape of the energy profile resembles the energy variation during oxygen ion migration via vacancies. The minimum energy is observed at 2.85 Å and equals 0 eV, indicating the position of the oxygen vacancy.

At other points, such as 1.2–1.4 Å, the energy reaches 0.92 and 0.90 eV, respectively, while near 3.65–3.85 Å, maxima of 0.99–1.01 eV are observed, despite the absence of direct interaction from the Mg atom. Further along, at 5.85–6.25 Å, the energy rises again to 0.94–1.12 eV.

This behavior indicates that the Mg atom, located outside the migration path, does not exert a significant stabilizing effect on the migration trajectory but does alter the electrostatic field. In contrast to the case where Mg ions are aligned along the migration path, the graph displays a sinusoidal pattern, and the peak energy values do not exceed 1.12 eV.
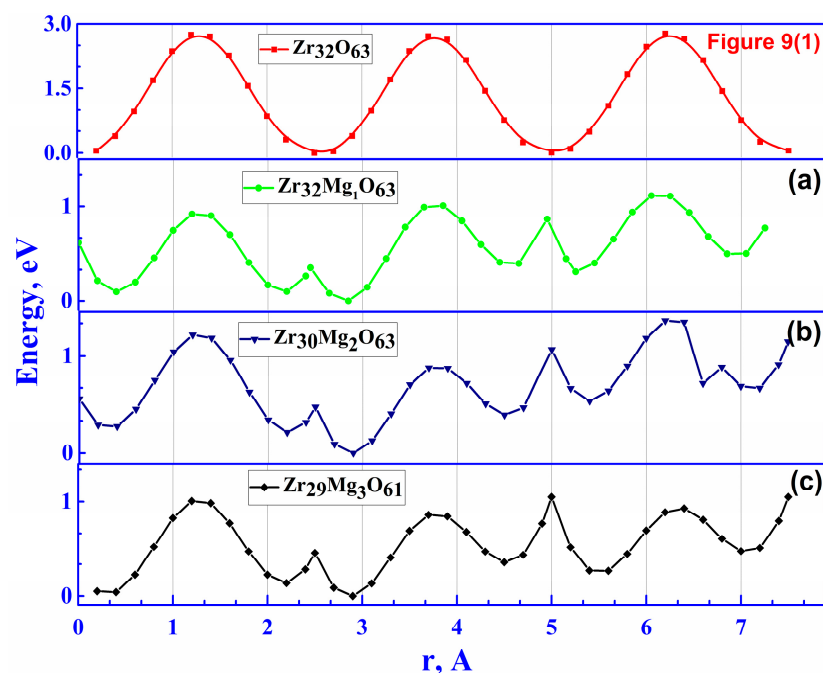
Figure 12. Dependence of the reduced total energy of the system during oxygen migration with substitution of one (**a**), two (**b**), and three (**c**) Zr atoms by Mg in c-ZrO$_2$. The top graph (previously labeled as Figure 9(1)) corresponds to the structure Zr$_{32}$O$_{63}$ with one oxygen vacancy.

Figure 12b shows the dependence of the reduced total energy of the system corresponding to the Zr$_{30}$Mg$_2$O$_{62}$ configuration, in which two magnesium atoms substitute zirconium atoms outside the migration path. At distances corresponding to the position of the vacancy, small potential barriers are observed. The minimum energy is reached at 2.9 Å and equals 0 eV, while the maximum occurs at distances of 1.2 Å (1.3 eV), 3.8 Å (0.85 eV), 5.0 Å (1.1 eV), 6.4 Å (1.3 eV), and 7.5 Å (1.1 eV). The placement of Mg^{2+} outside the migration path reduces the height of the energy barrier compared to when Mg^{2+} is located along the path.

Figure 12c shows the dependence of the reduced total energy of the system corresponding to the Zr$_{29}$Mg$_3$O$_{61}$ configuration. Here, three magnesium atoms substitute for zirconium outside the oxygen migration path. The energy along the trajectory fluctuates within 0.0–1.05 eV, with an absolute minimum at 2.9 Å (0 eV), corresponding to the position of the oxygen vacancy. Additional energy minima are observed at 0.2 Å (0.05 eV), 2.2 Å (0.13 eV), and 5.4–5.6 Å (~0.26 eV), indicating stabilization of the oxygen ion near these points. Maxima are observed at 1.2 Å (1.01 eV), 2.5 Å (0.5 eV), 3.7 Å (0.9 eV), 5.0 Å (1.05 eV), 6.4 Å (0.85 eV), and 7.5 Å (1.05 eV), indicating moderate energy barriers. Thus, introducing three Mg atoms outside the migration path preserves the symmetry of the electrostatic field and lowers the energy amplitude, providing a stable oxygen migration pathway.

The analysis of the influence of magnesium substitutions on the total energy of the oxygen migration system in the ZrO$_2$ structure has shown that the nature and effectiveness of the modification directly depend on both the number of Mg^{2+} ions and their spatial arrangement relative to the migration pathway.

When magnesium ions are located outside the migration trajectory, the variation in the normalized total energy becomes smooth, and the maximum energy barriers are 0.9 eV and 1.3 eV, respectively (Table 3). The results of the performed calculations show that the spatial positioning of the implanted magnesium ions outside the migration path significantly reduces the height of the potential barriers. Overall, increasing the number of Mg^{2+} ions, when optimally positioned either along or outside the trajectory, contributes to a decrease in the energy barriers.

Table 3. Energy Barriers for Oxygen Migration in c-ZrO$_2$ with Different Numbers and Positions of Mg Atoms.

Doping Configuration	Number of Mg	Min. Barrier, eV	Max. Barrier, eV
Zr$_{31}$Mg$_1$O$_{63}$	1	0.4	1.12
Zr$_{30}$Mg$_2$O$_{62}$	2	0.5	1.34
Zr$_{29}$Mg$_3$O$_{61}$	3	0.5	1.05

4. Discussion

The creation of a single oxygen vacancy in cubic ZrO$_2$ leads to the formation of defect levels within the band gap and a reduction in the energy barrier for oxygen ion migration. A particularly significant factor is the presence of lattice oxygen atoms along the migration pathway—when these are absent, the barrier is considerably reduced, facilitating ionic conductivity. These findings are consistent with theoretical studies that emphasize the critical role of vacancies in zirconia-based oxide systems [66,67].

When zirconium atoms are substituted with magnesium along the oxygen migration pathway, stable complex defects are formed, as evidenced by the consistent decrease in the system's total energy with increasing Mg content. However, the migration energy profiles exhibit a nonlinear dependence on the number and position of dopant atoms along the channel. For instance, with one Mg atom, a moderate reduction in the barrier to 1.27 eV is observed; with two Mg atoms, a sharp increase in the primary barrier to 3.03 eV occurs midway through the path; and with three Mg atoms, the most balanced behavior is achieved—a continuous channel is formed with nearly zero energy and moderate barriers of 0.96–1.32 eV, providing optimal conditions for migration. These differences are explained by local lattice distortions and charge redistribution induced by different doping configurations along the channel [68].

In contrast, substituting zirconium with magnesium outside the oxygen migration pathway also leads to a decrease in the system's total energy with increasing Mg content but does not cause significant changes in the migration energy landscape. With two and three substitutions outside the migration channel, the barriers remain moderate (with a maximum of 0.96–1.3 eV), the profile maintains symmetry, and no sharp local distortions are observed. This indicates that such doping exerts only a background electrostatic effect and smooths the potential landscape. Similar conclusions are presented in studies on the role of vacancies and their correlation with doping in oxide systems [67].

Table 4 summarizes the relative energies (ΔE) of different defect configurations in cubic ZrO$_2$, calculated with respect to the ideal Zr$_{32}$O$_{64}$ supercell. The results show that the creation of oxygen vacancies alone leads to an increase in the total energy, indicating destabilization of the structure. In contrast, substitution of Zr by Mg in combination with oxygen vacancies significantly lowers the system energy, thus stabilizing the defective configurations. A comparison between Mg atoms placed along the migration pathway and outside of it demonstrates that the "along pathway" configurations are slightly more favorable, with energy differences of less than 3 eV depending on the number of Mg substitutions.

In contrast, Mg substitution along with the migration trajectory can either enhance or hinder conductivity, depending on the number and distribution of the substitutions. Considering the experimental impossibility of aligning Mg substitutions strictly along a specific migration channel direction, the most effective approach is to introduce the maximum possible amount of Mg substitutions throughout the crystal volume in combination with oxygen vacancies. This strategy enables the formation of a continuous, energetically favorable path for oxygen migration. These conclusions align with computational results on perovskites, where the importance of coordinated defect structure tuning for achieving high ionic conductivity is emphasized [69], as well as with modeling studies demonstrating

the impact of rhodium and silver doping on oxygen behavior in oxide and perovskite systems [70–72], and the significance of the local electronic environment near vacancies and color centers in fluoride [73,74] and oxides [75–77].

Table 4. Total energies of the ZrO_2 system for different numbers of oxygen vacancies and Mg dopants (along and outside the migration pathway).

Configuration	Mg Position	Total Energy (eV)	$\Delta E = E_{config} - E_{Zr_{32}O_{64}}$ (eV)
$Zr_{32}O_{64}$		−171,752.37	0.00
$Zr_{32}O_{63}$		−169,742.54	+2009.83
$Zr_{32}O_{61}$		−165,599.06	+6153.31
$Zr_{31}Mg_1O_{63}$		−173,916.22	−2163.85
$Zr_{30}Mg_2O_{62}$	along pathway	−176,037.62	−4285.25
$Zr_{29}Mg_3O_{61}$		−178,159.57	−6407.20
$Zr_{31}Mg_1O_{63}$		−173,914.32	−2161.95
$Zr_{30}Mg_2O_{62}$	outside pathway	−176,034.90	−4282.53
$Zr_{29}Mg_3O_{61}$		−178,158.75	−6406.38

It should be noted that all calculations presented here were performed at 0 K and therefore do not account for the direct influence of thermal vibrations on the migration barriers. At elevated temperatures typical for solid oxide fuel cells (800–1200 K), thermal fluctuations reduce the absolute values of the barriers and accelerate oxygen transport. Nevertheless, as shown in molecular dynamics studies [78,79], the relative trends induced by defects and substitutions are preserved even at high temperatures. Therefore, the DFT results at 0 K can be regarded as a reliable baseline for analyzing the impact of vacancies and substitutions on ionic conductivity in ZrO_2.

5. Conclusions

The obtained results are of great importance for understanding the mechanisms of crystalline structure stabilization in ZrO_2 and can be applied in the development of materials for solid oxide fuel cells (SOFCs) and oxygen sensors.

Thus, the main objective of this study has been achieved. A fundamental relationship has been established between the number and spatial distribution of magnesium substitutions and the shape of the energy landscape for oxygen migration. The findings confirm that controlled defect distribution (vacancies and substitutions) is a key factor in optimizing ionic conductivity in zirconia, opening new prospects for the targeted design of solid oxide electrolytes and sensing materials.

Data Availability Statement: The data will be available upon request.

Conflicts of Interest: The authors declare no conflicts of interest.

Abbreviations

The following abbreviations are used in this manuscript:

DFT	Density functional theory
DOS	A function that describes the number of electronic states at each energy level that are available to be occupied in a system.
PDOS	A decomposition of the total DOS into contributions from specific atoms or orbitals helps to understand which atoms or orbitals contribute to particular energy levels.
B3LYP	A hybrid Density Functional Theory (DFT) functional that combines Becke's three-parameter exchange functional with the Lee-Yang-Parr correlation functional.

References

1. Danilov, V.P.; Borisova, E.S.; Shukshin, V.E.; Runina, K.I.; Strekalov, P.V.; Mayakova, M.N.; Petrova, O.B. Structure and optical properties of ZrO_2–Sc_2O_3 solid solution system obtained by the coprecipitation method. *Glass Ceram.* **2025**, *81*, 428–437. [CrossRef]
2. Sathya, A.; Anburaj, D.B.; Porkalai, V.; Muthuvel, A.; Al-Zaqri, N. Hydrothermal synthesis of ZrO_2 nanoparticles: Study on structural, optical, morphology properties, and photocatalyst activity. *Phys. Solid State* **2025**, *67*, 196–206. [CrossRef]
3. Fu, S.; Zhang, J.; Chen, X.; Wang, Z.; Zhao, Y. Oxygen defect-rich CeO_{2-x}@ZrO_2 Mott–Schottky electrocatalyst with tunable interfacial charge redistribution for accelerated sulfur redox kinetics in lithium–sulfur batteries. *Chem. Eng. J.* **2025**, *512*, 162371. [CrossRef]
4. Jin, H.-B.; Zhang, Z.-H.; Ma, P.; Li, H.-B. Synergically enhancing lithium-ion storage performance of silicon anode by designing shelled structure with reduced graphene oxide and ZrO_2. *Rare Met.* **2025**, *44*, 2393–2404. [CrossRef]
5. Jammee, R.; Kolganov, A.; Groves, M.C.; Pidko, E.A.; Sydora, O.L.; Conley, M.P. C–H bond activation by sulfated zirconium oxide is mediated by a sulfur-centered Lewis superacid. *Angew. Chem. Int. Ed.* **2024**, *63*, e202421699. [CrossRef]
6. Florez, J.; Diaz-Uribe, C.E.; Vallejo, W.; Duran, F.; Puello, E.; Salazar, J.; Zarate, X.; Schott, E. Study of methylene blue removal and photocatalytic degradation on zirconia thin films modified with Mn-Anderson polyoxometalates. *Dalton Trans.* **2025**, *54*, 2471–2482. [CrossRef] [PubMed]
7. Han, W.; Lin, L.; Cen, Z.; Ke, Y.; Xu, Q.; Zhu, J.; Mei, X.; Xia, Z.; Zheng, X.; Wang, Y.; et al. Production of branched alkanes by upcycling of waste polyethylene over controlled acid sites of SO_4/ZrO_2–Al_2O_3 catalyst. *Angew. Chem. Int. Ed.* **2025**, *64*, e202417923. [CrossRef]
8. Huang, Q.A.; Cao, Y.; Satou, K.; Murayama, H.; Yoshizawa, A.; Yamamoto, E.; Nakayama, A.; Ishida, T.; Kitagawa, Y.; Ishimaru, Y.; et al. Active and stable Au/ZrO2 catalysts for isomerization of allylic esters: A practical application of heterogeneous gold catalysis. *Appl. Catal. B Environ. Energy* **2025**, *373*, 125351. [CrossRef]
9. Yang, Z.; Liu, T.; Wang, H.; Zhang, Z.; Yin, H.; Wang, S.; Waterhouse, G.I.N.; Wang, X.; Ma, C.; Li, P. *Synergistic Adsorption-Catalysis Regulation Effect for Carbon Dioxide Over Hierarchically-Structured Cu/Zro2 Nts*; Elsevier: Amsterdam, The Netherlands, 2024.
10. Luo, J.; Yao, C.; Zhou, Y.; Qian, Y.; Wang, L.; Lu, C.; Li, X. Facile Oxygen Functionalization Strategy for Mediating the Activity–Stability Trade-Off for Metal Encapsulated Catalysts. *Surf. Interfaces* **2025**, *72*, 107209. [CrossRef]
11. Li, M.; Wang, S.; Dong, M.; Wang, J.; Fan, W. Effect of metal-support interaction on catalytic performance of Pd/ZrOx in CO_2 hydrogenation to formate. *Chem. Res. Chin. Univ.* **2025**, *41*, 529–538.
12. Lee, S.H.; Lee, T.Y.; Lim, H.H.; Cho, J.W.; An, C.; Chae, S.C. Symmetry engineering in antiferroelectric ZrO_2 thin films via split-up behavior. *ACS Appl. Electron. Mater.* **2025**, *7*, 2146–2152. [CrossRef]
13. Wang, J.; Yang, X.; Song, X.-F.; Li, C.; Zhu, H.-F. The influence of Ce element doping on the mechanical properties of ZrO_2 ceramic from first-principles calculations. *Solid State Ion.* **2025**, *424*, 116865. [CrossRef]
14. Yuan, J.; Dai, J.-Q.; Zhao, M.-W.; Zhong, Y.-Y.; Deng, D.-W. First-principles study on thermodynamic stability and electronic structures of the ferroelectric binary HfO_2 and ZrO_2 (001) polar surfaces. *Surf. Interfaces* **2025**, *42*, 105523. [CrossRef]
15. Kadyrzhanov, K.K.; Kozlovskiy, A.A.; Konuhova, M.; Popov, A.I.; Shlimas, D.D.; Borgekov, D.B. Determination of gamma radiation shielding efficiency by radiation-resistant composite ZrO_2–Al_2O_3–TiO_2–WO_3–Nb_2O_5 ceramics. *Opt. Mater.* **2024**, *154*, 115752. [CrossRef]
16. Kozlovskiy, A.L.; Konuhova, M.; Shlimas, D.I.; Borgekov, D.B.; Zdorovets, M.V.; Shakirziyanov, R.I.; Garanin, Y.A.; Volodina, N.O.; Popov, A.I. Study of the effect of nanostructured grains on the radiation resistance of zirconium dioxide ceramics during gas swelling under high-dose irradiation with helium ions. *ES Mater. Manuf.* **2024**, *24*, 1165. [CrossRef]
17. Kenzhina, I.E.; Kozlovskiy, A.L.; Begentayev, M.; Blynskiy, P.; Tolenova, A.; Popov, A.I. Study of phase transformations in ZrO_2 ceramics stabilized by Y_2O_3 and their role in changing strength characteristics and heat resistance. *Sustainability* **2025**, *17*, 4284. [CrossRef]

18. Kozlovskiy, A.L.; Konuhova, M.; Borgekov, D.B. Study of irradiation temperature effect on radiation-induced polymorphic transformation mechanisms in ZrO$_2$ ceramics. *Opt. Mater.* **2024**, *156*, 115994. [CrossRef]

19. Imanova, G. Modeling defect formation in nano-ZrO$_2$ under He and H$^+$ irradiation. *Mod. Phys. Lett. B* **2024**, *38*, 2450206. [CrossRef]

20. Costantini, J.M.; Gutierrez, G.; Lelong, G.; Guillaumet, M.; Rahman, M.M.; Yasuda, K. Raman spectroscopy study of damage in swift heavy ion-irradiated ceramics. *J. Raman Spectrosc.* **2022**, *53*, 1614–1624. [CrossRef]

21. Liu, Y.; Zhu, Y.; Shen, T.; Chai, J.; Niu, L.; Li, S.; Jin, P.; Zheng, H.; Wang, Z. Irradiation response of Al$_2$O$_3$–ZrO$_2$ ceramic composite under He ion irradiation. *J. Eur. Ceram. Soc.* **2021**, *41*, 2883–2891. [CrossRef]

22. Dauletbekova, A.; Zvonarev, S.; Nikiforov, S.; Akilbekov, A.; Shtang, T.; Karavannova, N.; Akylbekova, A.; Ishchenko, A.; Akhmetova-Abdik, G.; Baymukhanov, Z.; et al. Luminescence properties of ZrO$_2$:Ti ceramics irradiated with electrons and high-energy Xe ions. *Materials* **2024**, *17*, 1307. [CrossRef]

23. Bandarenka, H.; Burko, A.; Laputsko, D.; Dronina, L.; Kovalchuk, N.; Podelinska, A.; Shapel, U.; Popov, A.I.; Bocharov, D. Ultraviolet exposure improves SERS activity of graphene-coated Ag/ZrO$_2$ substrates. *Crystals* **2023**, *13*, 1570. [CrossRef]

24. Nikiforov, S.V.; Kortov, V.S.; Kiryakov, A.N.; Konev, S.F.; Men'shenina, A.A. Increasing the luminescence yield of zirconia. *Tech. Phys. Lett.* **2017**, *43*, 1074–1076. [CrossRef]

25. Swami, S.K.; Khan, J.I.; Dutta, V.; Lee, J.; Laquai, F.; Chaturvedi, N. Spray-deposited aluminum-doped zinc oxide as an efficient electron transport layer for inverted organic solar cells. *ACS Appl. Energy Mater.* **2023**, *6*, 2906–2913. [CrossRef]

26. Kate, R.S.; Deokate, R.J. Effect of cobalt doping on electrochemical properties of sprayed nickel oxide thin films. *Mater. Sci. Energy Technol.* **2020**, *3*, 830–839. [CrossRef]

27. Ricca, C.; Ringuedé, A.; Cassir, M.; Adamo, C.; Labat, F. A comprehensive DFT investigation of bulk and low-index surfaces of ZrO$_2$ polymorphs. *J. Comput. Chem.* **2015**, *36*, 9–21. [CrossRef] [PubMed]

28. Shin, H.; Benali, A.; Luo, Y.; Crabb, E.; Lopez-Bezanilla, A.; Ratcliff, L.E.; Jokisaari, A.M.; Heinonen, O. Zirconia and hafnia polymorphs: Ground-state structural properties from diffusion Monte Carlo. *Phys. Rev. Mater.* **2018**, *2*, 075001. [CrossRef]

29. Rajesh, G.; Akilandeswari, S.; Govindarajan, D.; Thirumalai, K. Enhancement of photocatalytic activity of ZrO$_2$ nanoparticles by doping with Mg for UV light photocatalytic degradation of methyl violet and methyl blue dyes. *J. Mater. Sci. Mater. Electron.* **2020**, *31*, 4058–4072. [CrossRef]

30. Marfin, A.Y.; Nikiforov, S.V.; Ananchenko, D.V.; Zyryanov, S.S.; Yakovlev, G.A.; Denisov, E.I. Thermoluminescence of monoclinic ZrO$_2$ after electron irradiation. *AIP Conf. Proc.* **2022**, *2466*, 030012.

31. Sredojević, D.; Lazić, V.; Pirković, A.; Periša, J.; Murafa, N.; Spremo-Potparević, B.; Živković, L.; Topalović, D.; Zarubica, A.; Krivokuća, M.J.; et al. Toxicity of silver nanoparticles supported by surface-modified zirconium dioxide with dihydroquercetin. *Nanomaterials* **2022**, *12*, 3195. [CrossRef]

32. Osinkin, D.A.; Antonova, E.P.; Lesnichyova, A.S.; Tropin, E.S.; Chernov, M.E.; Chernov, E.I.; Farlenkov, A.S.; Khodimchuk, A.V.; Eremin, V.A.; Kovrova, A.I.; et al. Application of promising electrode materials in contact with a thin-layer ZrO$_2$-based supporting electrolyte for solid oxide fuel cells. *Energies* **2020**, *13*, 1190. [CrossRef]

33. Qi, S.; Porotnikova, N.M.; Ananyev, M.V.; Kuzmin, A.V.; Eremin, V.A.; Pankratov, A.A.; Molchanova, N.G.; Reznitskikh, O.G.; Farlenkov, A.S.; Vovkotrub, E.G.; et al. High-temperature glassy-ceramic sealants SiO$_2$–Al$_2$O$_3$–BaO–MgO and SiO$_2$–Al$_2$O$_3$–ZrO$_2$–CaO–Na$_2$O for solid oxide electrochemical devices. *Trans. Nonferrous Met. Soc. China* **2016**, *26*, 2916–2924. [CrossRef]

34. Farlenkov, A.S.; Ananyev, M.V.; Eremin, V.A.; Porotnikova, N.M.; Kurumchin, E.K. Particle coarsening influence on oxygen reduction in LSM–YSZ composite materials. *Fuel Cells* **2015**, *15*, 131–139.

35. Nikiforov, S.; Dauletbekova, A.; Gerasimov, M.; Kasatkina, Y.; Denisova, O.; Lisitsyn, V.; Golkovski, M.; Akylbekova, A.; Bazarbek, A.-D.; Akilbekov, A.; et al. Thermoluminescent and dosimetric properties of zirconium dioxide ceramics irradiated with high doses of pulsed electron beam. *Crystals* **2023**, *13*, 1585. [CrossRef]

36. Ananchenko, D.V.; Nikiforov, S.V.; Sobyanin, K.V.; Konev, S.F.; Dauletbekova, A.K.; Akhmetova-Abdik, G.; Akilbekov, A.T.; Popov, A.I. Paramagnetic defects and thermoluminescence in irradiated nanostructured monoclinic zirconium dioxide. *Materials* **2022**, *15*, 8624. [CrossRef]

37. Borik, M.A.; Bredikhin, S.I.; Bublik, V.T.; Kulebyakin, A.V.; Kuritsyna, I.E.; Lomonova, E.E.; Milovich, P.O.; Myzina, V.A.; Osiko, V.V.; Ryabochkina, P.A.; et al. Structure and conductivity of yttria- and scandia-doped zirconia crystals grown by skull melting. *J. Am. Ceram. Soc.* **2017**, *100*, 5536–5547. [CrossRef]

38. Gayathri, P.; Balasubramani, V.; Balraju, P.; Sayed, M.A.; Shkir, M. Ultra-high photosensitivity response in MIS SBDs enabled by Zn-integrated ZrO$_2$@Zn interfacial layers for photovoltaic devices. *Phys. B Condens. Matter* **2025**, *714*, 417506.

39. Aboraia, A.M.; Sharaf, I.M.; Alradaddi, S.; Trabelsi, A.B.G.; Alkallas, F.H. Advanced supercapacitors benefit from the electrode material Gd-Enhanced Cubic-ZrO$_2$. *Phys. B Condens. Matter* **2025**, *714*, 417519.

40. Cheng, Z.; Ren, H.; Wang, Y.; Ta, S.; Zhang, P.; Yang, Y.; Xu, S.; Goodman, B.A.; Deng, W. Effects of Yb$_2$O$_3$ as stabilizer and sensitizer on the luminescence properties of cubic ZrO$_2$ single crystals. *Cryst. Growth Des.* **2022**, *22*, 5481–5488.

41. Thammachart, M.; Meeyoo, V.; Risksomboon, T.; Osuwan, S. Catalytic activity of CeO_2–ZrO_2 mixed oxide catalysts prepared via sol–gel technique: CO oxidation. *Catal. Today* **2001**, *68*, 53–61. [CrossRef]

42. Li, P.; Chen, I.-W.; Penner-Hahn, J.E. Effect of dopants on zirconia stabilization—An X-ray absorption study: II, tetravalent dopants. *J. Am. Ceram. Soc.* **1994**, *77*, 1281–1288. [CrossRef]

43. Winczewski, J.P.; Zeiler, S.; Gabel, S.; Maestre, D.; Merle, B.; Gardeniers, J.; Arce, A.S. Additive manufacturing of 3D yttria-stabilized zirconia microarchitectures. *Mater. Des.* **2024**, *238*, 112701. [CrossRef]

44. Feng, Y.; Wu, J.; Chi, Q.; Li, W.; Yu, Y.; Fei, W. Recent advances in design and applications of heteroatom-doped carbon with single-atom active sites. *Chem. Rev.* **2020**, *120*, 1710–1766. [CrossRef]

45. Haering, C.; Roosen, A.; Schichl, H.; Schnöller, M. Mechanical properties of tape-cast electrolyte substrates for solid oxide fuel cells. *Solid State Ion.* **2005**, *176*, 261–268. [CrossRef]

46. King, A.; Singh, R.; Anand, R.; Behera, S.K.; Nayak, B.B. Phase and luminescence behaviour of Ce-doped zirconia nanopowders for latent fingerprint visualisation. *Optik* **2021**, *242*, 167087. [CrossRef]

47. Xie, Y.; Ma, Z.; Liu, L.; Su, Y.; Zhao, H.; Liu, Y.; Zhang, Z.; Duan, H.; Li, J.; Xie, E. Enhanced photocatalytic activity in ZrO_2–TiO_2 nanocomposite films deposited by magnetron sputtering. *Appl. Phys. Lett.* **2010**, *97*, 141916. [CrossRef]

48. Furasova, A.D.; Ivanovski, V.; Yakovlev, A.V.; Milichko, V.A.; Vinogradov, V.V.; Vinogradov, A.V. Inkjet fabrication of highly efficient luminescent Eu-doped ZrO_2 nanostructures. *Nanoscale* **2017**, *9*, 13069–13078. [CrossRef] [PubMed]

49. Winczewski, J.; Herrera, M.; Cabriel, C.; Izeddin, I.; Gabel, S.; Merle, B.; Arce, A.S.; Gardeniers, H. Additive manufacturing of 3D luminescent ZrO_2:Eu^{3+} architectures. *Adv. Opt. Mater.* **2022**, *10*, 2102758. [CrossRef]

50. Kurakhmedov, A.E.; Morzabayev, A.K.; Tleubay, I.; Berguzinov, A.; Kozlovskiy, A.L. Study of the mechanisms of polymorphic transformations in zirconium dioxide upon doping with magnesium oxide, as well as establishing the relationship between structural changes and strength properties. *Ceramics* **2023**, *6*, 1164–1178. [CrossRef]

51. Malyi, O.I.; Wu, P.; Kulish, V.V.; Bai, K.; Chen, Z. Formation and migration of oxygen and zirconium vacancies in cubic zirconia and zirconium oxysulfide. *Solid State Ion.* **2012**, *212*, 117–122. [CrossRef]

52. Kurakhmedov, A.E.; Alin, M.; Temir, A.M.; Ivanov, I.A.; Bikhert, Y.V.; Ungarbayev, Y.O.; Zdorovets, M.V.; Kozlovskiy, A.L. Study of the effect of doping ZrO_2 ceramics with MgO to increase the resistance to polymorphic transformations under the action of irradiation. *Nanomaterials* **2021**, *11*, 3172. [CrossRef]

53. Perevalov, T.V.; Islamov, D.R. Oxygen polyvacancies as conductive filament in zirconia: First principle simulation. *ECS Trans.* **2017**, *80*, 357–362. [CrossRef]

54. Xue, Q.; Huang, X.; Wang, L.; Zhang, H.; Zhang, J. Computational and experimental investigations of defect interaction and ionic conductivity in doped zirconia. *Phys. Rev. Appl.* **2018**, *10*, 014032. [CrossRef]

55. Dhingra, A.; Thakur, O.P.; Pandey, R. Structure–property relationship and electronic structure calculation of cubic YSZ solid electrolyte for electrochemical applications. *J. Electron. Mater.* **2025**, *54*, 1949–1960. [CrossRef]

56. Hohenberg, P.; Kohn, W. Inhomogeneous electron gas. *Phys. Rev.* **1964**, *136*, B864–B871. [CrossRef]

57. Kohn, W.; Sham, L.J. Self-consistent equations including exchange and correlation effects. *Phys. Rev.* **1965**, *140*, A1133–A1138. [CrossRef]

58. Becke, A.D. Density-functional thermochemistry. III. The role of exact exchange. *J. Chem. Phys.* **1993**, *98*, 5648–5652. [CrossRef]

59. Lee, C.; Yang, W.; Parr, R.G. Development of the Colle–Salvetti correlation-energy formula into a functional of the electron density. *Phys. Rev. B* **1988**, *37*, 785–789. [CrossRef]

60. Erba, A.; Desmarais, J.K.; Casassa, S.; Civalleri, B.; Dona, L.; Bush, I.J.; Searle, B.; Maschio, L.; Edith-Dazr, L.; Cossard, A.; et al. CRYSTAL23: A program for computational solid-state physics and chemistry. *J. Chem. Theory Comput.* **2022**, *19*, 6891–6932. [CrossRef]

61. Muhammad, I.D.; Awang, M. Modelling the interatomic potential of cubic zirconia. *Appl. Mech. Mater.* **2013**, *446–447*, 151–157. [CrossRef]

62. French, R.H.; Glass, S.J.; Ohuchi, F.S.; Xu, Y.-N.; Ching, W.Y. Experimental and theoretical determination of the electronic structure and optical properties of three phases of ZrO_2. *Phys. Rev. B* **1994**, *49*, 5133–5142. [CrossRef] [PubMed]

63. Kröger, F.A. *The Chemistry of Imperfect Crystals*, 2nd ed.; North-Holland Publishing Company: Amsterdam, The Netherlands, 1974; Volume 2.

64. Li, W.; Sunarso, J.; Yang, Y.; Chen, Y.; Ge, C.; Wang, W.; Guo, Y.; Ran, R.; Zhou, W. Strategies for improving oxygen ionic conducting in perovskite oxides and their practical applications. *Energy Rev.* **2024**, *3*, 100085. [CrossRef]

65. Rauf, S.; Hanif, M.B.; Mushtaq, N.; Tayyab, Z.; Ali, N.; Shah, M.Y.; Javed, Q.; Rasool, K.; Khan, M.A.; Xu, W. Modulating the energy band structure of the Mg-doped $Sr_{0.5}Pr_{0.5}Fe_{0.2}Mg_{0.2}Ti_{0.6}O_{3-\delta}$ electrolyte with boosted ionic conductivity and electrochemical performance for solid oxide fuel cells. *ACS Appl. Mater. Interfaces* **2022**, *14*, 43067–43084. [CrossRef] [PubMed]

66. Kulish, V.V.; Malyi, O.I.; Persson, C.; Wu, P. Evaluation of phosphorene as anode material for Na-ion batteries: A first-principles study. *Phys. Chem. Chem. Phys.* **2015**, *17*, 13921–13928. [CrossRef]

67. Hinuma, Y.; Graciani, J.; Stacchiola, D.; Senanayake, S.D.; Rodríguez, J.A.; Ganduglia-Pirovano, M.V. Density functional theory calculations of oxygen vacancy formation and subsequent molecular adsorption on zirconia surfaces. *J. Phys. Chem. C* **2018**, *122*, 1687–1696. [CrossRef]

68. Han, Z.-K.; Liu, W.; Gao, Y. Advancing the understanding of oxygen vacancies in ceria: Insights into their formation, behavior, and catalytic roles. *JACS Au* **2025**, *5*, 1549–1569. [CrossRef]

69. Emery, A.A.; Wolverton, C. High-throughput DFT calculations of formation energy, stability, and oxygen vacancy formation energy of ABO_3 perovskites. *Sci. Data* **2017**, *4*, 160124. [CrossRef]

70. Kaptagay, G.A.; Satanova, B.M.; Abuova, A.U.; Konuhova, M.; Zakiyeva, Z.Y.; Tolegen, U.Z.; Koilyk, N.O.; Abuova, F.U. Effect of rhodium doping for photocatalytic activity of barium titanate. *Opt. Mater. X* **2025**, *25*, 100382. [CrossRef]

71. Inerbaev, T.M.; Abuova, A.U.; Zakiyeva, Z.Y.; Abuova, F.U.; Mastrikov, Y.A.; Sokolov, M.; Gryaznov, D.; Kotomin, E.A. Effect of Rh doping on optical absorption and oxygen evolution reaction activity on $BaTiO_3$ (001) surfaces. *Molecules* **2024**, *29*, 2707. [CrossRef]

72. Abuova, A.U.; Mastrikov, Y.A.; Kotomin, E.A.; Kawazoe, Y.; Inerbaev, T.M.; Akilbekov, A.T. First-principles modeling of Ag adsorption on the $LaMnO_3$ (001) surfaces. *Solid State Ion.* **2015**, *273*, 46–50. [CrossRef]

73. Abuova, F.U.; Kotomin, E.A.; Lisitsyn, V.M.; Akilbekov, A.T.; Piskunov, S. Ab initio modeling of radiation damage in MgF_2 crystals. *Nucl. Instrum. Methods Phys. Res. Sect. B Beam Interact. Mater. At.* **2014**, *326*, 314–317. [CrossRef]

74. Dauletbekova, A.; Abuova, F.; Akilbekov, A.; Kotomin, E.; Piskunov, S. First-principles modeling of the H color centers in MgF_2 crystals. *Phys. Status Solidi C* **2013**, *10*, 160–164. [CrossRef]

75. Zhukovskii, Y.F.; Platonenko, A.; Piskunov, S.; Kotomin, E.A. Ab initio simulations on migration paths of interstitial oxygen in corundum. *Nucl. Instrum. Methods Phys. Res. Sect. B Beam Interact. Mater. At.* **2016**, *374*, 29–34. [CrossRef]

76. Kaewmeechai, C.; Strand, J.; Shluger, A.L. Structure and migration mechanisms of oxygen interstitial defects in β-Ga_2O_3. *Phys. Status Solidi B* **2025**, *263*, 2400652. [CrossRef]

77. Usseinov, A.B.; Akilbekov, A.T.; Kotomin, E.A.; Karipbayev, Z.T. First-principles calculations of CO_2 adsorption on the (10-10) ZnO surface. *AIP Conf. Proc.* **2019**, *2174*, 020181. [CrossRef]

78. Kilo, M.; Argirusis, C.; Borchardt, G.; Jackson, R.A. Oxygen diffusion in yttria-stabilised zirconia—Experimental results and molecular dynamics calculations. *Phys. Chem. Chem. Phys.* **2003**, *5*, 2219–2224. [CrossRef]

79. Momenzadeh, L.; Belova, I.V.; Murch, G.E. Analysis of thermotransport and thermal and ionic conductivity in doped lanthanum gallate (LSGM) using molecular dynamics. *Solid State Ion.* **2022**, *377*, 115881. [CrossRef]